Author/s:
Othman, M;Zheng, F;Seeber, A;Chesman, ASR;Scully, AD;Ghiggino, KP;Gao, M;Etheridge, J;Angmo, D

Title:
Millimeter-Sized Clusters of Triple Cation Perovskite Enables Highly Efficient and Reproducible Roll-to-Roll Fabricated Inverted Perovskite Solar Cells

Date:
2022-03-01

Citation:
Othman, M., Zheng, F., Seeber, A., Chesman, A. S. R., Scully, A. D., Ghiggino, K. P., Gao, M., Etheridge, J. & Angmo, D. (2022). Millimeter-Sized Clusters of Triple Cation Perovskite Enables Highly Efficient and Reproducible Roll-to-Roll Fabricated Inverted Perovskite Solar Cells. Advanced Functional Materials, 32 (12), https://doi.org/10.1002/adfm.202110700.

Persistent Link:
https://hdl.handle.net/11343/299294

Millimeter-sized Clusters of Triple Cation Perovskite Enables Highly Efficient and Reproducible Roll-to-Roll Fabricated Inverted Perovskite Solar Cells

Mostafa Othman, Fei Zheng, Aaron Seeber, Anthony S. R. Chesman, Andrew D. Scully, Kenneth P. Ghiggino, Mei Gao, Joanne Etheridge, Dechan Angmo**

M. Othman, Dr. A. Seeber, Dr. A. S. R. Chesman, Dr. A. D. Scully, Dr. D. Angmo

Devices and Engineered Systems, Manufacturing

Commonwealth Scientific and Industrial Research Organization

Victoria 3168, Australia

Email: Dechan.Angmo@csiro.au

M. Othman, Prof. J. Etheridge

Department of Materials Science and Engineering and ARC Centre of Excellence in Exciton Science

Monash University

Victoria 3800, Australia

Email: joanne.etheridge@monash.edu

Prof. J. Etheridge

Monash Centre for Electron Microscopy

Monash University

Victoria 3800, Australia

This is the author manuscript accepted for publication and has undergone full peer review but has not been through the copyediting, typesetting, pagination and proofreading process, which may lead to differences between this version and the Version of Record. Please cite this article as doi: 10.1002/adfm.202110700.

Dr. Fei Zheng and Prof. Ken Ghiggino

School of Chemistry and ARC Centre of Excellence in Exciton Science

The University of Melbourne

Victoria 3010, Australia

Dr. A. S. R. Chesman

Melbourne Centre for Nanofabrication

Australian National Fabrication Facility

Victoria 3168, Australia

Abstract

The high-power conversion efficiencies (PCEs) of perovskite solar cells (PSCs) on lab-scale devices triggers the need to develop scalable manufacturing processes to accelerate their commercialisation transition. A roll-to-roll (R2R) vacuum-free printing on flexible substrates allows for high-volume and low-cost manufacturing which is especially well-suited for PSCs due to its solution processibility and low temperature annealing requirements. Herein, a facile hot deposition technique is reported to fabricate triple-cation ($Cs_{0.07}FA_{0.79}MA_{0.14}Pb(I_{0.83}Br_{0.17})_3$) perovskite films in an ambient environment using a R2R slot-die coating method. This perovskite composition, whilst being most studied in lab devices due to its high efficiency and stability, has not been applied in R2R fabrication thus far. The demonstrated R2R slot-die coated flexible PSCs achieve stabilized PCE reaching 12% at maximum power point in inverted 'p-i-n' architectures, the highest efficiency reported to date for R2R inverted PSCs. To achieve this, the underlying hole transport layer (PEDOT:PSS) is modified with guanidium iodide (GAI) additive which leads to the formation of large milli-metre sized perovskite clusters, improved perovskite crystallinity, and enhanced charge-transfer efficiency. This study highlights the potential of the facile hot-deposition method while providing critical insights into the role of

interfacial engineering in eliminating performance losses and fabricating efficient printed flexible PSCs.

1. Introduction

Organic-inorganic metal halide perovskite materials have generated enormous interest due to their simple processing requirements[1–5] and superior opto-electronic properties including band-gap tunability[6], strong light absorption[7], high charge mobility[8] and long carrier diffusion lengths.[9] The record laboratory-scale power conversion efficiency (PCE) for single-junction perovskite solar cells (PCSs) has recently reached 25.5%, rivalling most of the established photovoltaic (PV) technologies such as silicon (Si), copper indium gallium selenide (CIGS), and cadmium telluride (CdTe)-based solar cells.[10] With the unique combination of these favourable characteristics and rapid progress, PSCs have the potential to be a cost-competitive clean energy technology. To accelerate the commercialization of PSCs, the development of industrially-compatible large-scale manufacturing processes are required.[11–16]

Among the myriad possible production methods, roll-to roll (R2R) manufacturing on low-cost flexible substrates using solution-based coating and printing deposition methods allows high-volume and low-cost manufacturing. Such a R2R scheme is especially suited for PSCs due to their solution processibility and low-temperature annealing requirements. Various scalable fabrication techniques such as inkjet printing[17], slot-die coating (SDC)[18], doctor-blading[19] and gravure printing[20] have been successfully utilised for the deposition of perovskite films. Notably, SDC is the most facile and scalable technique that allows in-situ patterning and control of coating characteristics, such as wet layer thickness and coating width using printing parameters such as the web speed, solution flow rate, and coated width.[21] Thus, SDC has yielded promising results in the deposition of perovskite films and others functional layers comprising a PSC on flexible substrates using R2R set-up under ambient conditions.[22–25]

Among all the functional layers comprising PSCs, the perovskite layer is the most challenging to fabricate a uniform film in continuous large-scale production. This is because many processes that are reported to generate uniform perovskite films in the laboratory require an inert environment using the non-scalable spin-coating methods. These processes often cannot be directly transferred to R2R procesing due to the sensitivity of perovskite films to moisture during crystallization [26–28] and the dynamic nature of film formation in spin-coating, which cannot be replicated by scalable methods such as slot-die coating.[29–31] Thus, a substantial amount of work is required to re-optimise and re-configure processes such that they can be made compatible with ambient fabrication conditions using scalable printing and coating methods.

Achieving uniform films was one of the earliest challenges in the development of PSCs at the laboratory-scale, which led to numerous approaches to generate high quality films with full surface coverage by controlling nucleation and crystal growth. Some of the these approaches are gas-quenching[32], anti-solvent treatment[33], the two-step sequential deposition method[[34]] and hot-deposition.[35] While many of these methods have been adapted to R2R manufacturing, the hot-deposition method is arguably the most appealing for several reasons.[16,25,36,37] Firstly, the hot-deposition is suited to most perovskite compositions in an economical one-step process.[38] Secondly, it is a facile approach that requires only a pre-heated substrate and/or solution immediately prior to/during deposition at a temperature optimized for a specific perovskite composition.[39–41] Thirdly, the simple one-step precursor solution allows room for additive engineering to further improve coating unformity.

To date, R2R fabrication has been reported for basic perovskite formulations such as $MAPbI_3$[42], $MAFAPbI_3$[43] and $CsFAPbI_3$[44], especially in planar 'n-i-p' structures. A table collating research on R2R devices is presented in **Supplementary Table 1**. Arguably, the most promising bulk perovskite composition is a mixed-cation mixed-halide such as $Cs_{0.07}FA_{0.79}MA_{0.14}Pb(I_{0.83}Br_{0.17})_{3,}$ first reported by Saliba *et* al., yet there are no reports of scalability for this formulation.[45] Based on our experience, this formulation is extremely difficult to process through nitrogen blowing or anti-solvent methods under ambient environments. In this work, we employ the hot-deposition technique for this perovskite composition in an inverted 'p-i-n' structure. A p-i-n architecture is preferable to an n-i-p architectures due to their long-term operational lifetimes, versatile fabrication techniques, and low-temperatures processing routes.[46–49] However, p-i-n exhibit inferior PCE values compared to n-i-p architectures due to non-radiative recombination and open-circuit voltage (V_{OC}) losses which limit the device performance.[50–52]

To mitigate these detrimental effects, we fabricated R2R flexible PSCs (f-PSCs) in p-i-n architectures by doping the guanidium iodide (GAI) additive into a poly(3,4-ethylenedioxythiophene) polystyrene sulfonate (PEDOT:PSS) hole transport layer as an interface modifier. This modification improves coating uniformity of subsequently R2R-coated perovskite film, enhances perovskite crystallinity, increases perovskite cluster size, supresses surface defects, and improves charge extraction, thereby leading to improved optoelectronic properties and photovoltaic device performance. This passivation strategy yields a champion PCE of ~12% on an active area of 0.20 cm^2 for R2R p-i-n PSC devices, which is the highest reported for p-i-n structures in general and for a mixed-cation mixed-halide perovskite composition in particular.

2. Results and Discussion

A p-i-n device architecture was used in this study for the following reasons: p-i-n devices can be manufactured at low temperatures (≤ 140 °C), which lie within the thermal tolerance of plastic substrates such as the polyethylene terephthalate (PET) films commonly used in R2R coating[53], their ease of fabrication[54], and charge transport layers (CTLs) in p-i-n architectures are comparatively less absorptive than n-i-p ones, which reduces the risk of potential performance losses during device operation.[55] **Figure 1a** illustrates the employed device configuration; PET/indium-doped tin oxide (ITO) /PEDOT:PSS/perovskite/phenyl-C61-butyric-acid-methyl-ester (PCBM)/polyethylenimine ethoxylated (PEIE)/gold (Au). The 3D perovskite absorber layer was based on the mixed-cation mixed-halide formulation ($Cs_{0.07}FA_{0.79}MA_{0.14}Pb(I_{0.83}Br_{0.17})_3$) (referred to as CsMAFA, where Cs is cesium, MA is methylammonium and FA is formamidinium) with a 3 mole %

excess of PbI_2 and a small amount of L-α-phosphatidylcholine surfactant to aid in surface coverage.[22] Herein, we utilized a hot-deposition technique for the perovskite film fabrication at ambient environmental conditions as shown schematically in **Figure 1b**. A photograph of the slot-die coating station where the perovskite solution is undergoing hot-deposition and a corresponding video of the process are shown in **Figure 1c** and **Supplementary Video 1**.

We optimized the deposition temperatures in terms of film quality. Hot-deposited perovskite films are characterized by micron-sized clusters, a repetitive feature comprising of radially arranged submicron grains. Unlike anti-solvent and nitrogen-blowing processes, the hot-deposited film quality can be easily checked with an optical microscope due to the large-size of the clusters **(Supplementary Figure 1)**. These clusters have been referred to as grains in the literature, which is a misnomer.[35] The optical images of films fabricated at 90 °C show isolated 10-20 µm clusters emanating from nucleation sites. The size of these clusters increases in size with increasing temperature until they coalesce at 130-140 °C. Additionally, the slot-die coating parameters such as web speed and flow rate were optimized for the fabrication of perovskite films.

The morphology of the films was examined using SEM as shown in **Supplementary Figure 2**. The formation of large clusters having average sizes of 50 – 100 µm was observed for flow rates of 10, 20, 25 and 30 µL min^{-1}**.** At higher flow rates of 40 and 50 µL min^{-1}, SEM images show an unusual morphology with an undulating surface, which indicates solution overflow and poor crystallization. A flow rate of 25 µL min^{-1} was found to produce the best device performance metrics, with reproducible V_{OC}, short-circuit current density (J_{SC}), fill factor (FF) and PCE values of 0.93 V, 21.7 mA cm^{-2}, 49 % and 10.1 %, respectively **(Figure 1(d-g))**. At increased flow rates, FF and J_{SC} values decrease leading to reduced PCE.

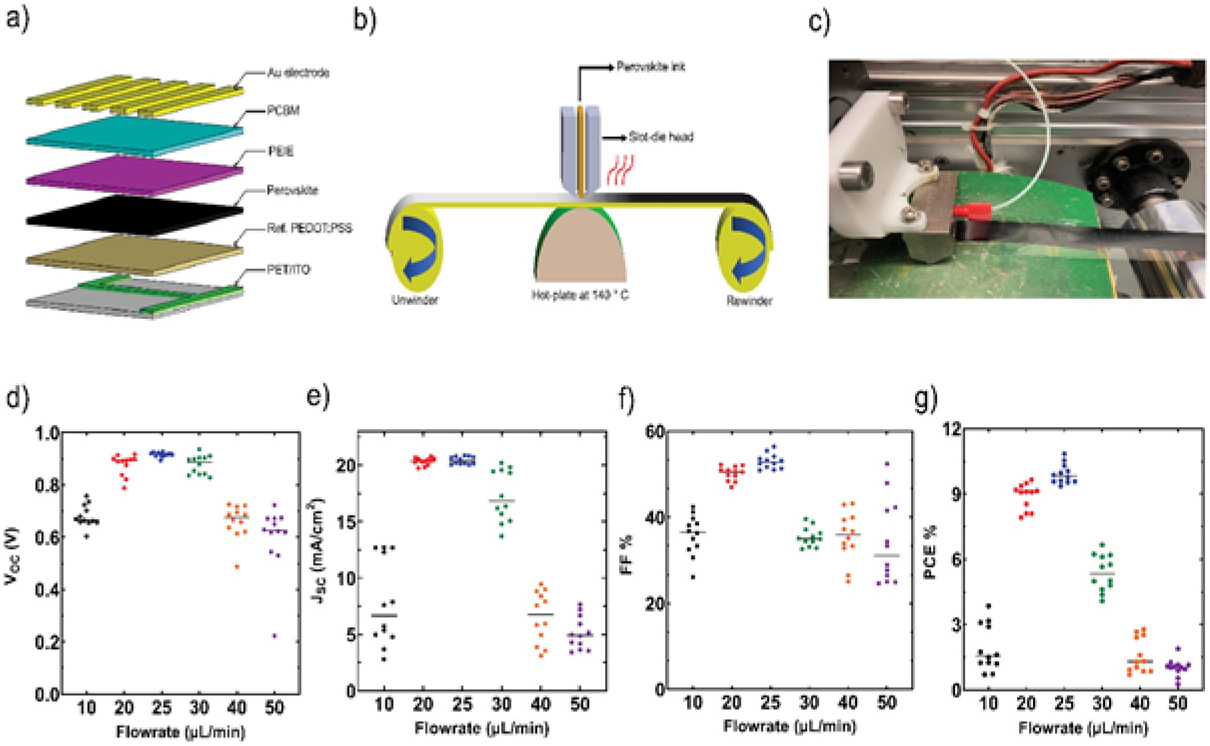

Figure 1. a) Scheme depicting the device layout of the p-i-n PSC, b) schematic of the employed hot deposition technique for perovskite film fabrication, c) View of the slot-die coating station featuring perovskite hot deposition, statistical distribution of the photovoltaic device performance parameters: d) V_{OC}, e) J_{SC}, f) FF and g) PCE. The data are based on the J-V results from 12 cells in a reverse scan direction at a scan rate of 20 mV s^{-1}.

The main limitation of the reference devices originated from significant losses in V_{OC} (~ 0.9 V) and FF (~ 50 %) which have been widely attributed to non-radiative recombination pathways present at the interface between the perovskite and CTLs.[56–59] The non-radiative recombination centres act as defect states that trap charge carriers during device operation, thus impairing the solar cell performance.[60] Therefore, we doped GAI as an additive into PEDOT:PSS (Modified PEDOT:PSS) for the dual-function of suppressing interfacial recombination and modifying interface energetics, while simultaneously allowing efficient charge (hole) extraction to the HTL. GA is a relatively large organic cation composed of three amino groups (—NH_2) with an ionic radius of ~ 278 nm; the amino group of the GA organic species is proposed to strengthen the hydrogen-bond formation with the undercoordinated iodine species of the perovskite phase, which would help to passivate surface defects.[61] Passivation of perovskite films with GAI and other alkyl ammonium compounds is a common approach reported in the literature.[62–65] However, these passivation materials are usually spin-coated on top of the perovskite film at high speed with a diluted alkyl ammonium solution in isopropyl alchohol (IPA). We attempted to apply GAI through this common approach in R2R using sequential slot-die coating, but found that IPA causes degradation of the perovskite. Upon deposition, IPA's dwell time on the perovskite film is significantly shorter in spin-coating where drying and film spreading occurs simultaneously due to the high angular acceleration. However, in R2R slot-die coating, film spreading and drying are discrete and slower processes, which causes a longer dwell time of the IPA on the underlying perovskite film, resulting in degradation of the perovskite film. In order to mitigate this, we investigated if we can harness the passivation effect of GAI by incorporating it into the underlying PEDOT:PSS layer.

The doping effect of GAI into PEDOT:PSS was first systematically analysed for ITO glass-based devices while maintaining the same device architecture used in R2R coating. An 8 mg mL^{-1} concentration was found to be optimum **(Supplementary Figure 3)**. The modified PEDOT:PSS was then transferred to the R2R process with the device structure shown in **Figure 2a** and complete devices were fabricated with R2R hot-deposition of perovskite film, spin-coating of PCBM and PEIE, and evaporation of gold electrode. The devices were compared nd compared against reference PEDOT:PSS based-devices fabricated along the same print length. **Figures 2b and c** shows the current-density voltage (J-V) curves of the best performing reference and modified PEDOT:PSS PSCs in both reverse (from V_{OC} to J_{SC}) and forward (from J_{SC} to V_{OC}) scan directions. The corresponding PV parameters are summarized in **Table 1**. The reference device showed a PCE in reverse scan mode of 10.1 % with a V_{OC} of 0.93 V, a J_{SC} of 21.7 mA cm^{-2} and a FF of 49 %, whereas the modified PEDOT:PSS devices showed an increase in the PCE to 11.9 % with a V_{OC} value of 0.95 V, J_{SC} value of 22 mA cm^{-2} and FF value of 57 %. The external quantum efficiency (EQE) for each PSC is presented in **Supplementary Figure 4.** The integrated J_{SC} calculated from the EQE spectra with respect to the AM1.5G solar spectrum was 19.04 and 20.12 mA cm^{-2} for both the reference and modified PEDOT:PSS devices, respectively, with a discrepancy < 8 % with those J_{sc} values determined from the J-V curves. We note that EQE J_{sc} measurements were carried out on unencapsulated cells in air. The modified PEDOT:PSS PSCs exhibited lower hysteresis than the reference ones between the reverse and forward scans as evident from the J-V curves. To further investigate the effect of this hysteresis in real world device performance, we measured maximum power point (MPP). **Figure 2d** shows MPP tracking for the modified and reference devices. The modified PEDOT:PSS PSC displayed a sharp rise and stabilized output of 11.9 %, which is the same value as the PCE observed in the reverse J-V scan, demonstrating better interfacial contact and excellent photostability.[66–68] However, the reference devices showed a slower rise to MPP and reached only 9.5 % PCE for the same time interval, suggesting higher resistive interfaces. MPP tracking over 2000 minutes (33 hours) showed promising stability with negligible degradation (**Supplementary Figure S5**). Long term stability tracking will be reported in a separate study. We note that the device area used for this study was 0.20 cm^2, which is twice the area commonly reported in other R2R literature.[37] Increasing the device area on flexible substrates leads to higher power losses compared with increasing the device area on glass/ITO substrates, due to the higher sheet resistance of the former (50 ohms sq^{-1}) compared to the latter (5 ohms sq^{-1}). Therefore, achieving a record PCE of ~12% after incurring higher power losses compared to other studies is notable. Achieving the highest efficiency record for R2R processed inverted perovskite with the current perovskite formulation represents substantial progress in lab-to-fab translation of PSCs.

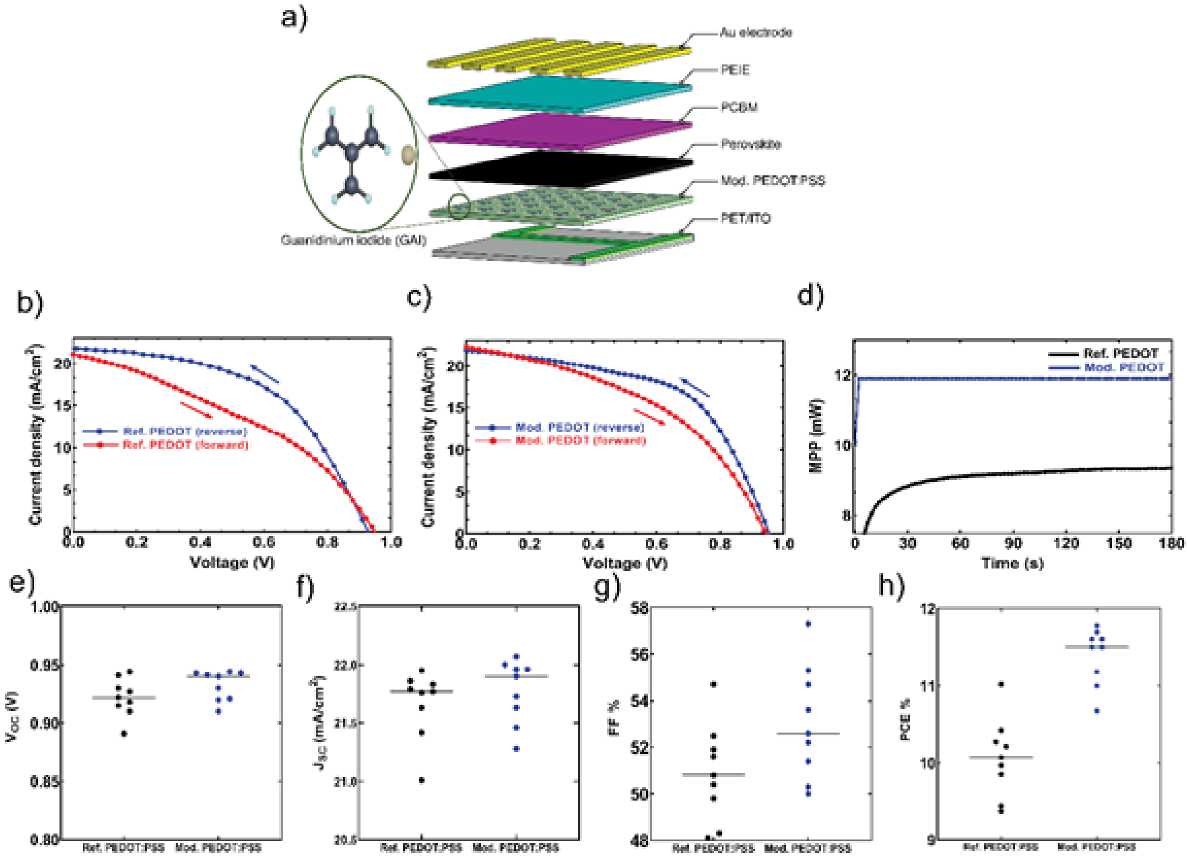

Figure 2. a) Schematic illustration of the device stack demonstrating the modified PEDOT:PSS PSC device**,** J-V curves of the best performing devices on: b) Reference PEDOT:PSS, c) Modified PEDOT:PSS, (d) Maximum power point (M_{PP}) tracking measured for both the reference and modified PEDOT:PSS devices, Scatter plots comparing the distribution of various photovoltaic parameters of reference and modified PEDOT:PSS based-devices: e) V_{OC}, f) J_{SC}, g) FF and h) PCE. All J-V data are measured under 1000 W m^{-2} (AM1.5G). Scatter plot data are based on 9 randomly selected cells measured in reverse scan direction at a scan rate of 20 mV s^{-1}.

The distribution of the device performance was further ascertained by measuring 9 devices fabricated randomly from printed reference and modified PEDOT:PSS PSC segments (**Figure 2(e-h)).**

Modified PEDOT:PSS devices show improved mean values of all the parameters. FF showed the most increase in value, implying reduced transport series resistance at the perovskite and modified PEDOT:PSS interface.[69] Most notably, the mean PCE of modified PEDOT:PSS devices was 11.4%, which is significantly superior to the previously reported highest mean value of 10.2% on half the device area.[22] A low standard deviation of <5% is achieved indicating high reproducibility.

Table 1. Champion PV parameters and hysteresis index of the inverted PSCs in different scan directions under standard 1 Sun illumination (100 mW cm^{-2})

Device	Scan direction	V_{OC} [V]	$V_{OCmean a)}$ [V]	J_{SC} [mA cm-2]	$J_{SCmean a)}$ [mA cm-2]	FF [%]	$FF_{mean a)}$ [%]	PCE [%]	$PCE_{mean a)}$ [%]	Hysteresis index$^{b)}$ (HI)
Reference PEDOT: PSS	Reverse	0.93	0.914 ± 0.012	21.7	21.67 ± 0.27	49	50.9 ± 1.97	10.1	10.07 ± 0.48	25.90
	Forward	0.94		21.1		43		7.48		
Modified PEDOT: PSS	Reverse	0.96	0.94 ± 0.01	22	21.78 ± 0.26	57	53.0 ± 2.28	11.9	11 .39 ± 0.35	15.10
	Forward	0.95		22.34		46		10.1		

a) The values in parentheses are the average from 9 devices with the standard deviation.

b) $\mathrm{HI} = \frac{\mathrm{PCE_{reverse}} - \mathrm{PCE_{forward}}}{\mathrm{PCE_{reverse}}}$

We further translated all four solution-based functional layers, namely, modified PEDOT:PSS, perovskite, PCBM, and PEIE, through R2R process and achieved a maximum PCE of 11.95% with optimization of PEIE coating condition (**Supplementary Figure S6**). The PCE value is same as in devices in which PCBM and PEIE are spin-coated as described earlier, which suggest that PCBM and PEIE coating quality achieved from spin-coating can be attained in R2R slot-die coating.

The perovskite films in the reference PEDOT:PSS devices started to show obvious degradation by turning into a yellowish color shortly after fabrication when left in air **(Supplementary Figure S7)**. This yellowing starts to take place from the edge of the print width where there is no ITO but only PEDOT:PSS, suggesting this perovskite composition has poor adhesion to PEDOT:PSS/PET. In contrast, the modified PEDOT:PSS/perovskite films maintained the black perovskite color with no signs of degradation, suggesting the GAI doping into PEDOT:PSS leads to better interfacial contact between perovskite and PEDOT:PSS and PEDOT:PSS/PET.

To understand the enhanced PV performance induced by GAI doping into PEDOT:PSS, we examined the possible underpinning morphological, structural, photophysical and electronic reasons driving this improvement for the perovskite films and devices. Scanning Electron Microscope (SEM) was used to investigate the effect of the GAI additive in PEDOT:PSS on the morphology of the overlying hot-deposited perovskite films (slot-die coated). As shown in **Figure 3a and b,** the reference film displays a polycrystalline pin-hole free morphology with large grain clusters of about 600 – 700 µm, while the modified film demonstrates a significant enlargement in the grain clusters with average sizes of 800 µm – 1 mm. Such large clusters have been previously only reported with spin-coated devices at higher temperatures of 190 °C to 200 °C.[35] However, such a high temperature cannot be applied for R2R fabrication on low-cost flexible PET substrates due to PET’s thermal tolerance limit of 140 °C. Thus, we moved our fabrication to a humidity-controlled laboratory and devices were R2R fabricated in an environment with a relative humidity between 25-35% and temperature of 23-25 °C. This led to significant improvement in the cluster size reaching up-to 1 mm at a hot-deposition temperature of 140 °C compared to those fabricated under an uncontrolled environment with relative humidity of 40-50% with clusters rarely larger over 200 µm observed. Larger clusters mean fewer grain boudaries, which is beneficial for charge transport in devices.[70] We also note that the clusters are fused together without any gaps between them. The gap between clusters is a recurring defect in hot-deposited perovskite films which can short devices. The addition of a small amount of surfactant eliminates this defect.[22]

X-ray diffraction (XRD) measurements were performed to analyze the phases and crystallinity of the perovskite films **(Figure 3c and d).** The samples were from the same batch as those examined by SEM. Perovskite films on modified PEDOT:PSS and reference PEDOT:PSS exhibit the typical 001, 011, 111 and 002 perovskite peaks corresponding to the metrically cubic phase of mixed-cation mixed-halide composition (due to the nominally irrational stoichiometry, the structure cannot have a cubic space group).[71] In addition, the reference film shows stronger intensities for diffraction peaks associated with the yellow photo-inactive δ-$FAPbI_3$ and PbI_2 phases at 11.6° and 12.6° respectively, in comparison to the perovskite film on modified PEDOT:PSS, which indicates a reduction in these contaminant phases upon PEDOT:PSS modification.[72] The presence of impurities such as MFAI or DMFAI could cause the slight left shift in δ-$FAPbI_3$ from the expected 11.72° to 11.6° [73]. Overall, the XRD result suggests that GAI doping into PEDOT:PSS may participate in the control of the perovskite crystallization process reducing impurity phases. In addition, the full-width at half-maximum (FWHM) values of the 001 perovskite peak were 0.16° and 0.10° for the perovskite films on reference and modified PEDOT:PSS, respectively, suggesting that GAI additive enhances the crystallinity of the perovskite crystal **(Figure 3d).**

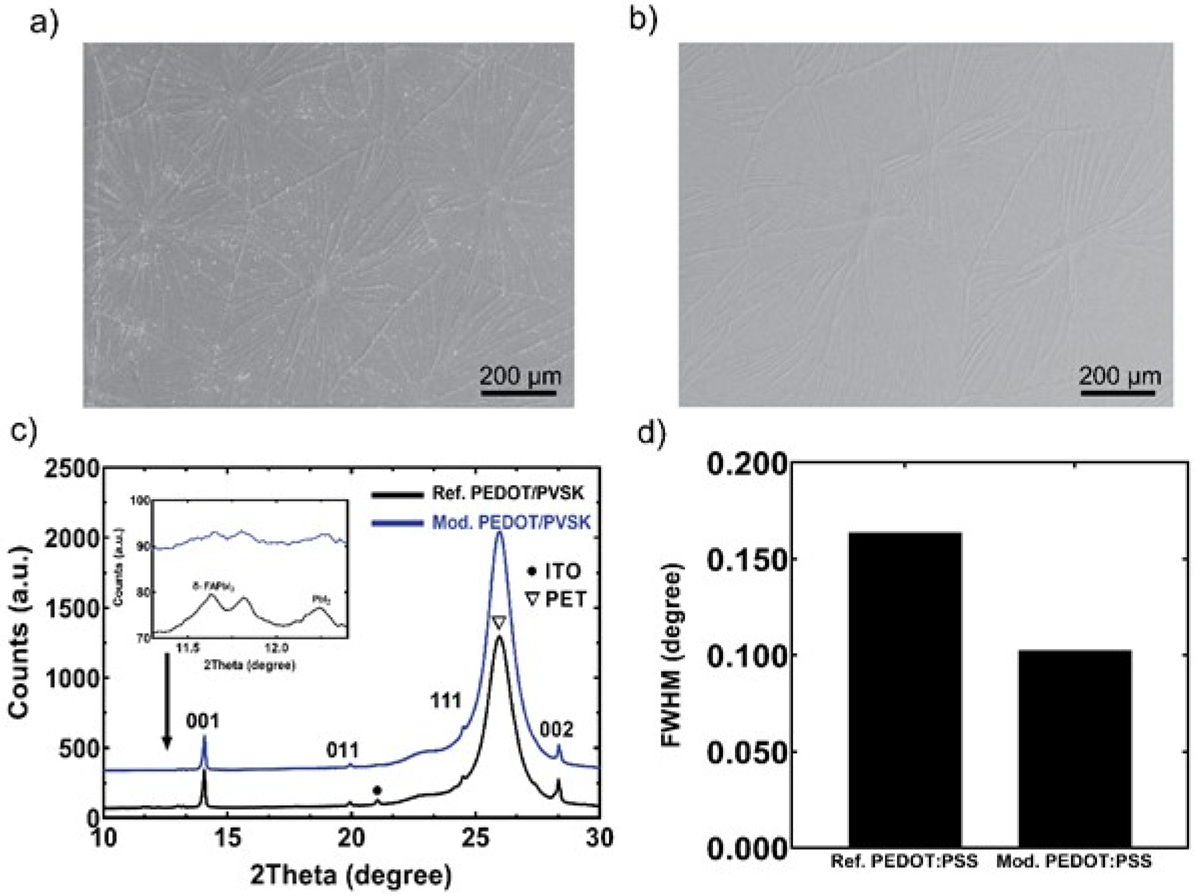

Figure 3. SEM micrographs of the perovskite films on: a) Reference PEDOT:PSS, b) Modified PEDOT:PSS, c) XRD patterns of the reference and modified PEDOT:PSS perovskite films and d) FWHM of the of the 001 perovskite peak at 14.1° for the reference and modified films.

To characterize the crystallinity and domain orientation of the perovskite films slot-die coated on control and modified PEDOT:PSS/PET substrates, grazing incidence wide-angle X-ray scattering (GIWAXS) was conducted with an incident angle of 0.1°, for which the 2D scattering patterns are shown in **Figures 4a and b,** respectively. The discrete large spots appearing in both samples are associated with the background scattering from the uncovered PET substrate.[74] The sharp concentric scattering rings are attributed to the reflections by the randomly oriented crystallites within the 3D perovskite films, which is consistent with literature reports.[75] To quantitatively evaluate the influence of PEDOT:PSS modification on the crystallinity of the printed perovskite films, sector integrations along the in-plane (horizontal) and out-of-plane (vertical) directions were performed, giving the diffraction intensity profiles as shown in **Figures 4c and d.** The broad diffraction peaks at q=1.16 Å^{-1} (in-plane plots) and q=1.84 Å^{-1} (out-of-plane plots) correspond to the scattering from PET. The peaks at q=1.00 Å^{-1}, 1.43 Å^{-1}, 2.01 Å^{-1}, and 2.25 Å^{-1} obtained from both the in-plane and out-of-plane diffraction profiles of the pervoskite films on reference and modified PEDOT:PSS can be assigned to the 001, 112, 002, and 114 diffraction peaks of the mixed cations and halides perovskite phases ($Cs_{0.07}FA_{0.79}MA_{0.14}Pb(I_{0.83}Br_{0.17})_3$), respectively.[76] There is a significant increase in the diffraction intensity for the perovskite film on modified PEDOT:PSS compared to the perovskite film on reference PEDOT:PSS suggesting preferential orientation. The diffraction peaks originating from the unreacted PbI_2 (q=0.92 Å^{-1}) observed in the control film disappear in the modified sample.[77] Intermediate solvate phases ($MAI.PbI_2.DMSO$) signals at q= 0.5 and 0.47 Å^{-1} observed in the perovskite film on reference PEDOT:PSS are not present in the perovskite film on modified PEDOT:PSS, suggesting GAI promotes the perovskite crystallization formation through rapid removal of undesired solvent complexes.[77–79] These results further support the distinct enhancement of perovskite crystallinity upon the modification of PEDOT:PSS hole transporting layer.

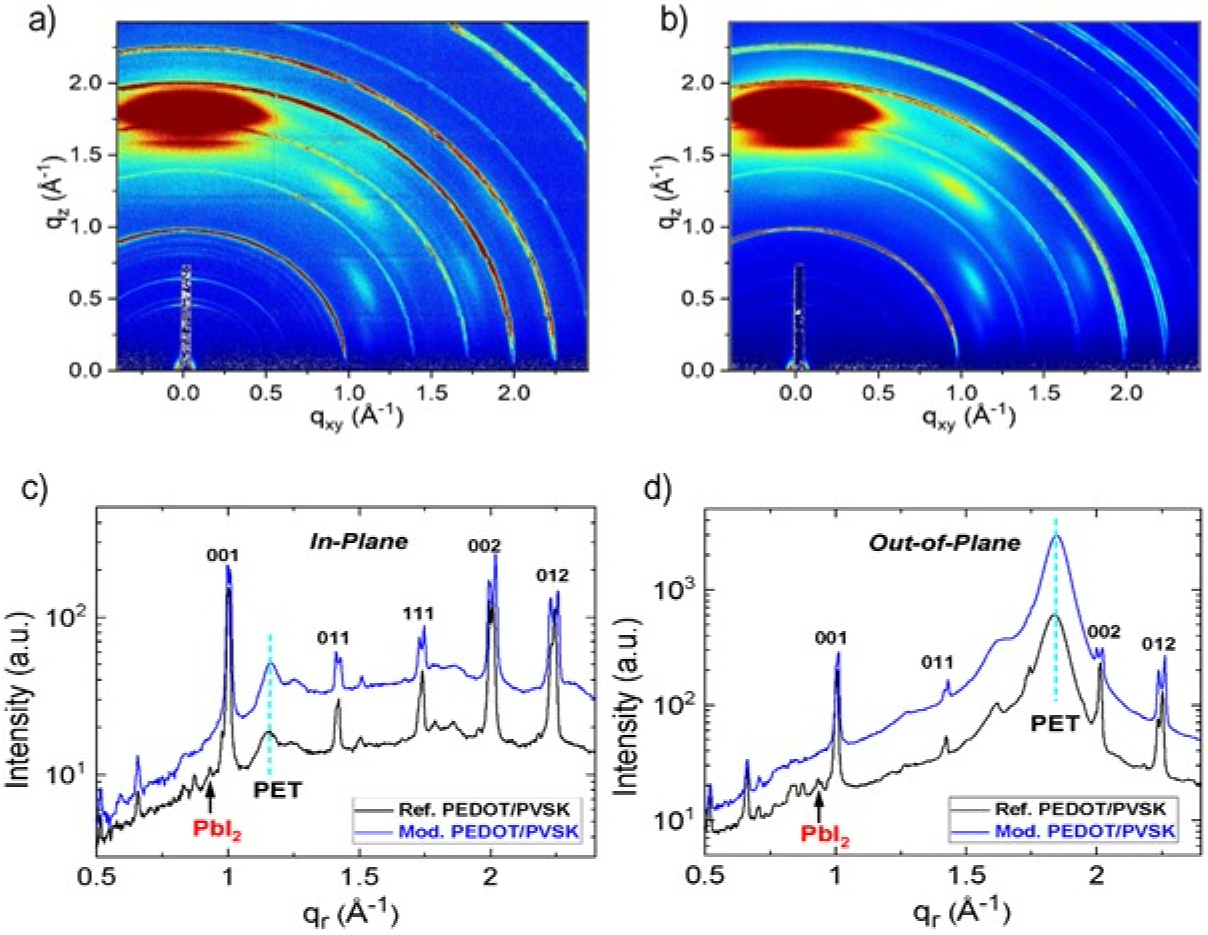

Figure 4. 2D GIWAXS scattering patterns: a) Reference, b) Modified printed perovskite films on PEDOT:PSS/PET substrates, The corresponding sector integrated diffraction intensity profiles along the c) in-plane and d) out-of-plane directions.

Ultraviolet-visible (UV-Vis) absorption spectroscopy was used to study the band gap of the films **(Figure 5a)**. The bandgap of the perovskite films is essentially independent of PEDOT:PSS modification having an absorption onset at 844 nm (1.47 eV). Notably, this is a reduction in the bandgap value commonly reported for the same mixed-cation mixed-halide perovskite formulation made in an inert environment, which is tentatively attributed to the different crystallization dynamics at ambient conditions.[80–82] The perovskite film on the modified PEDOT:PSS shows a slight dip in absorption in the longer wavelength region between 600-725 nm, the origin of which is unknown. UV-vis spectra of the two different PEDOT:PSS layers perfectly overlap, ruling out the possibility that parasitic absorption of PEDOT:PSS modification with GAI is responsible for the dip in the absorption (**Supplementary Figure S8).** Thus, the dip is likely associated with the different quality of the perovskite film formed on the modified PEDOT:PSS film. Despite this dip, the J_{SC} of the perovskite film on the modified PEDOT:PSS is enhanced compared to the film on the reference PEDOT:PSS, suggesting negligible deleterious effect of the reduced absorption on the perovskite on modified PEDOT:PSS.

Photoluminscence (PL) spectra and decay curves were investigated to study the charge-carrier dynamics in the perovskite films. As demonstrated in **Figures 5b and 5c,** the PL intensity and PL lifetime of the perovskite film on a modified PEDOT:PSS is strongly quenched compared to the perovskite film on reference PEDOT:PSS, implying enhanced rate of hole extraction by the modified PEDOT:PSS. The PL decay curves were fitted using a bi-exponential decay function[84,85]:

$$I(t) = A_1 \exp\left({}^{-\tau}/_{\tau_1}\right) + A_2 \exp({}^{-\tau}/_{\tau_2})$$

To a first approximation, the decay kinetics of the faster decaying component (τ_1) is influenced mainly by the rate of hole-transfer from the perovskite film to the PEDOT:PSS layer, while at the low excitation fluence used in this work the slower component (τ_2) is assigned to trap-mediated recombination in the bulk perovskite film. The best-fit parameter values for the decay curves in Figure 5c are given in **Supplementary Table S2**. The best-fit values for τ_1 values for the reference and modified PEDOT:PSS hole-transport layers are 113 ns and 46 ns, respectively, which is consistent with enhanced rate of hole-transfer for the later.

Photoluminescence microscopy was used to investigate the opto-electronic quality of the perovskite films on the different PEDOT:PSS and the presence of any spatial inhomogeneities. The PL images shown in **Figure 5d and e** are taken at the edge of the ITO. Thus, half of the PL image is with the structure incorporating ITO (i.e. PET/ITO/modified or reference PEDOT:PSS/perovskite), while other half of the image is without ITO (PET/modified or reference PEDOT:PSS/perovskite) as indicated on the image. A schematic illustration is provided in **Figure 5f** to guide the location of the imaged area.

Figure 5d shows PL images for the PEDOT:PSS and perovskite interface through PET/ITO. Perovskite films on ITO with both modified and reference PEDOT:PSS are quenched as evident in reduced PL intensity of the region on ITO compared to their respective region without ITO. The PL image of the perovskite film on ITO/reference PEDOT:PSS shows some inhomogeneity evident as dark spots, while the perovskite film shows greater inhomogeneity in regions without the ITO with faded cluster boundaries and the presence of high PL intensity speckles (**Figure 5d)**. In contrast, the PL image of perovskite film on modified PEDOT:PSS shows similar homogenity in regions with and without ITO.

Figure 5e shows the PL images captured from perovskite/air inteface. Two observations can be made. Firstly, the perovskite film on reference PEDOT:PSS shows homogenous PL unlike the opposite interface shown in **Figure 5d**, which suggests poor adhesion of the perovskite on reference PEDOT:PSS is responsibile for the defects and inhomogeneities observed at the opposite perovskite/PEDOT:PSS interface. The PL image supports the observation pertaining to film quality and degradation from edges previously discussed in relation **to Supplementary Figure S7**. Secondly, there is no contrast between ITO and non ITO regions in the perovskite on reference PEDOT:PSS, suggesting poor hole transfer from the top perovskite surface. On the other hand, the perovskite film on modified PEDOT:PSS show similar homogeneity and contrast in ITO vesus non-ITO regions compared to the opposite interface discussed in **Figure 5d**, suggesting improved charge transfer across the bulk thickness. Thus, the PL image results further supports the findings from the steady-state PL and TRPL data where modified PEDOT:PSS was found to enable improved hole transfer.

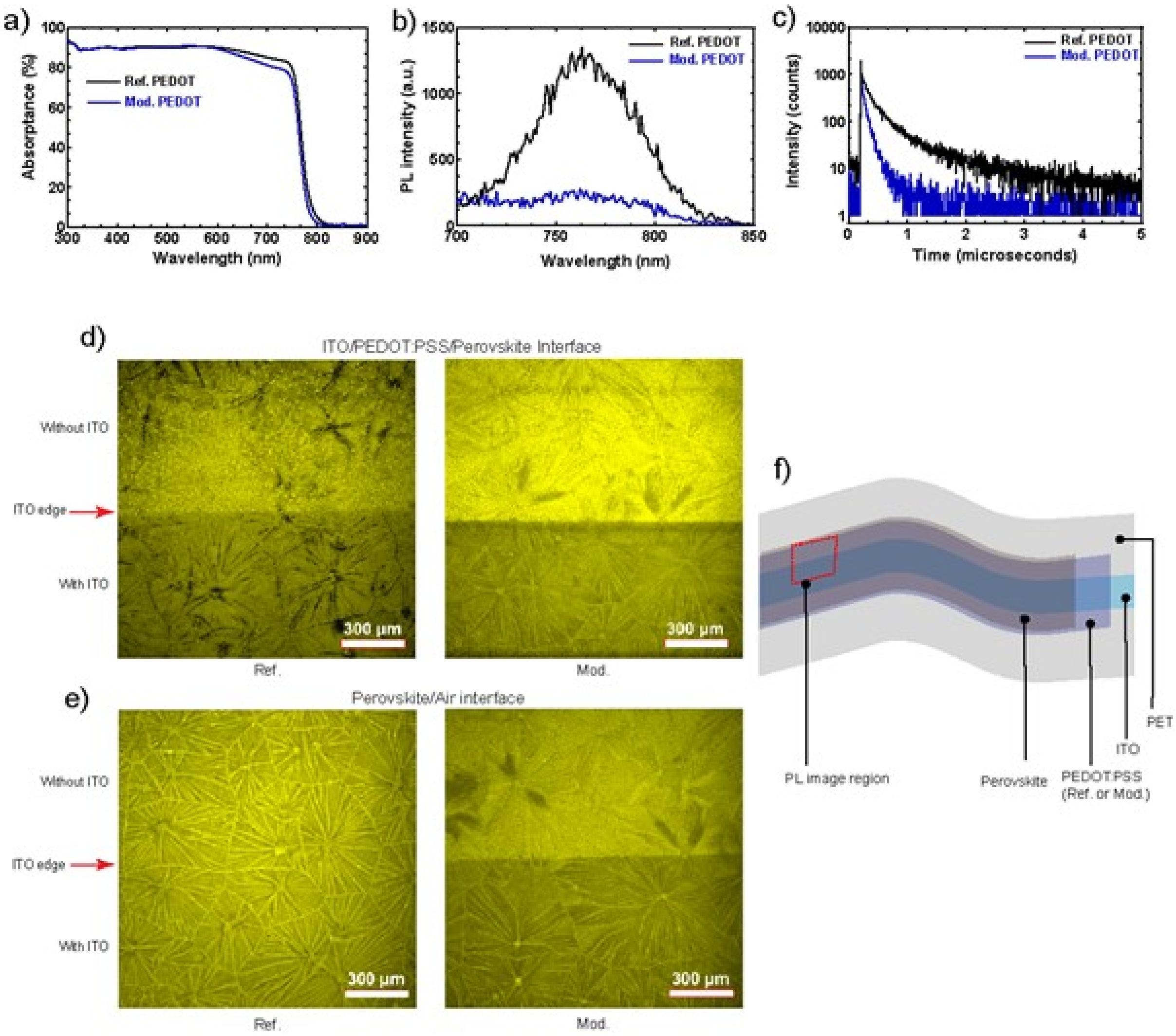

Figure 5. Optoelectronic properties of the perovskite films (sample structure: PET/ITO/Ref. Or Mod. PEDOT:PSS/Perovskite): a) UV-Vis absorption spectra, b) PL emission spectra (ex 466 nm), c) PL decay curves (ex 466 nm, em 770 nm), PL imaging for the films at different interfaces: d) PET side, e) Air side and f) Schematic respresenting the PL imaging mechanism.

To investigate the origin of the improved hole transfer for perovskite films on modified PEDOT:PSS, the electronic structure of the films was assessed by ionization potential measurements using photo-electron spectroscopy-in-air (PESA). From the fitted PESA data, the valence band maxima (VBM) was evaluated for the perovskite, reference and modified PEDOT:PSS films to be 5.25, 4.94 and 4.74 eV, respectively **(Figure 6 (a-c)).** These findings confirm that GAI doping results in a decrease of the energy band offset between the perovskite and ref. PEDOT:PSS VBMs by 200 meV, which led to reduced V_{oc} losses, thus yielding better interfacial energy alignment for holes extraction.[86] It is widely reported that smaller band offsets facilitate charge carriers extraction and suppress surface recombination losses.[88–92] Given the calculated perovskite band gap from UV-Vis absorption and VBM from PESA, the conduction band minima (CBM) was determined to be 3.78 eV. The final energy level diagram for the device is shown in **Figure 6d.**

We further conducted morphological characteristics of the PEDOT:PSS with and without GAI doping to understand what causes the the improvements observed in overlying perovskite film and its opto-electronics characteristics with the doping of GAI in the underlying PEDOT:PSS layer. SEM, atomic force microscopy (AFM) images, and contact angle measurements were conducted on R2R slot-die coated PEDOT:PSS with and without GAI (**Supplementary Figure 9**). SEM showed no signficant difference between the morphology of PEDOT:PSS with and without GAI doping. AFM images further confirmed negligible difference in the surface characteristics of PEDOT:PSS with and without GAI doping with a average surface roughness of 0.63 nm and 0.78 nm, respectively. Additionally, contact angle measurement of perovskite precursor solution on R2R printed HTL were similar with a value of 10.91^{o} for Ref. PEDOT:PSS and 10.55^{o} for Mod. PEDOT:PSS. Thus, the improvements in adhesion, cluster size, and electronic properties observed in perovskite film with underlying GAI Mod. PEDOT:PSS is likely to result from chemical interactions. As noted earlier, the amino group in GA is likely to strengthen the hydrogen-bond formation between the metal halide framework and the ammonium ions on the GA species, which can influence morphology and adhesion of the overlying perovskite layer.[61]

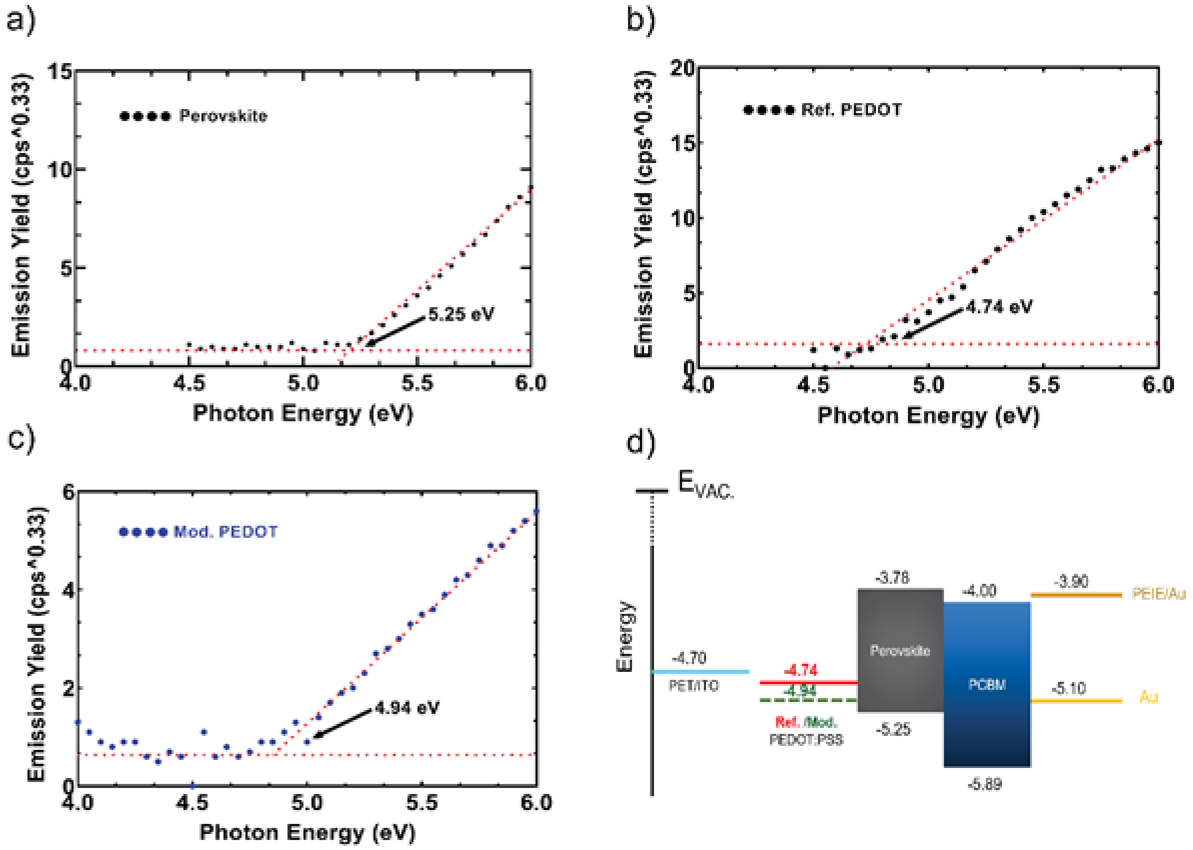

Figure 6. PESA measurements for the films: a) Perovskite, b) Reference PEDOT:PSS and c) Modified PEDOT:PSS and d) Energy-level diagram for the full device.

3. Conclusions

In summary, we have demonstrated the successful translation of a mixed-cation mixed-halide perovskite formulation ($Cs_{0.07}FA_{0.79}MA_{0.14}Pb(I_{0.83}Br_{0.17})_3$) from the laboratory to an industrially-relevant R2R fabrication method under an ambient environment through a facile hot-deposition process. We have further shown a novel passivation strategy for charge transport layers through the doping of PEDOT:PSS with the GAI additive to deliver improved photovoltaic performance of R2R air-processed f-PSCs. With an optimized GAI concentration (8 mg mL^{-1}), we achieved significant enhancements in V_{OC} and FF values from 0.93 to 0.95 V and 49 % to 57 %, respectively, leading to the realization of a stabilized power of ~12% on an active area of 0.2 cm^2, in a p-i-n architecture. This represents a new PCE record for slot-die coated R2R processed mixed-cation mixed-halide f-PSCs fabricated in ambient conditions. In-depth structural, morphological, and optoelectronic analyses have yielded a thorough understanding of the origins of these improvements in device performance. Futhermore, the highly reproducible device performance metrics represent an important step forward on the goal towards developing stable and scalable coating protocols for f-PSCs. This work provides a new avenue towards scalable low-cost and efficient f-PSC technology. Further studies targeting many important aspect of upscaling such as scalability and impact of solution aging are crucial for pushing the efficiency limits and practical deployment of these solar cells.

4. Experimental Section

Materials. Formamidinium iodide (FAI), methylammonium bromide (MABr) and guanidinium iodide (GAI) were purchased from Greatcell Solar Materials, lead iodide (PbI_2) and lead bromide ($PbBr_2$) were purchased from Alfa Aesar, cesium iodide (CsI), anhydrous dimethylformamide (DMF), anhydrous dimethylsulphoxide (DMSO), anhydrous chlorobenzene (CBZ) and anhydrous iso-propanol (IPA) were purchased from Sigma-Aldrich. PEDOT:PSS (Baytron P AI 4083) was purchased from HC Starck and polystyrene sulfonate (MW ~70,000) was purchased from Sigma-Aldrich. $PC_{61}BM$ (99%) was purchased from Ossila. Polyethyleneimine ethoxylated (PEIE) was purchased from Sigma Aldrich.

Solution preparation. Reference PEDOT:PSS solution was prepared by mixing 1 mL PEDOT:PSS (Baytron P Al 4083), 60 mg sodium polystyrene sulfonate (molecular weight ~70,000, Sigma-Aldrich), and 5 mL deionized water followed by stirring overnight. Before use, the solution was filtered through a 0.20 µm regenerated cellulose syringe filter. The modified PEDOT:PSS was prepared using the exact same procedure for the reference except with the addition of 10 µL from a solution of 8 mg mL^{-1} GAI dissolved in IPA after filtering the PEDOT:PSS solution. The 3D perovskite precursor solution was prepared in a N_2-filled glovebox by mixing 1.12M PbI_2, 1.1M FAI, 0.19M MABr and 0.2M PbBr powders in 1mL of anhydrous N,N-dimethylformamide (DMF) and dimethyl sulfoxide (DMSO) (4:1 v/v) with a final concentration of 1.4M. The solution contains 3 mol % excess PbI_2. 34 µL of CsI dissolved in DMSO (1.5 M) was then added to the precursor solution. The perovskite precursor solution was left to stir overnight until fully dissolved. Before use, 20 ppm of L-α-phosphatidylcholine surfactant from a 2 mg/ml stock solution in DMF was added to improve the film wettability. For the electron transport layer solution, 12 mg of $PC_{61}BM$ was dissolved in 1mL of CBZ. For PEIE, 30 µL of the solution was diluted in 10 mL anhydrous IPA followed by sonication for 30 seconds.

Roll-to-roll fabrication on PET flexible substrates. All the roll-to-roll experiments were conducted under ambient environment conditions with film deposition carried out using slot-die coating to produce the PEDOT:PSS and perovskite films, respectively. The PEDOT:PSS precursor solutions were slot-die coated at a flow rate of 25 µL min^{-1} and web speed of 0.35 m min^{-1} at a coating bed temperature of 70 °C. The coated films were further dried by passing under hot air oven at 120 °C followed by a hot-plate mounted in the R2R line at 140 °C. The coated films turn a dark bluish color upon these drying steps. The substrate was then rewound to the starting point for perovskite coating. For perovskite film deposition, the substrate was preheated at 140 °C at slot-die coating parameters of 25 µL min^{-1} flow rate and 0.2 m min^{-1} web speed followed by further annealing at 100 °C for ~ 2 seconds per substrate. Then the films were cut to spin-coat $PC_{61}BM$ and PEIE on top of the perovskite films. 80 µL of $PC_{61}BM$ was spin-coated using a 3 step program, first step was 3000 rpm with a ramping speed of 10,000 rpm for 30 seconds, second step was 0 rpm with a ramping speed of

10,000 rpm for 5 seconds and at this step 50 µL of PEIE was spin-coated followed by a final step of 5000 rpm with a ramping speed of 10,000 rpm for 20 seconds. Finally, the device fabrication was completed by depositing 80 nm thin layer of gold (Au) electrode using thermal evaporation. For all R2R processed devices, PCBM was slot-die coated at a temperature of 70 C with 30 µL min^{-1} flow rate and 0.4 m min^{-1} web speed. PEIE coating condition was optimised as shown in Figure S6.

Materials characterization.

UV-Vis absorptance: The transmittance (T) and reflectance (R) spectra were measured using a Lambda 1050 spectrophotometer equipped with a 150 mm InGaAs integrating sphere (PerkinElmer, Glen Waverly, Australia). With these two measurements, the absorptance (A) was calculated as as A = 1 – T(%) – R(%).. All samples were fabricated using roll-to-roll slot-die coating on flexible PET substrates

SEM: Taken with a Zeiss Merlin field emission SEM (FE-SEM) operated at an accelerating voltage of 5 kV. Images were acquired using an In-lens detector and a working distance of 5 mm. Prior to imaging, a 5 nm layer of Ir was sputter-coated.

Optical microscopy images: Acquired in bright field mode using an Olympus BX61 microscope.

XRD: A Bruker D8 Advance A25 X-ray Diffractometer operating under CuKα radiation (40kV, 40mA) equipped with a Lynx Eye XE-T detector was employed to obtain the X-ray diffractograms. The samples were scanned over the 2θ range 10° to 30° with a step size of 0.02° and a count time of 0.8 second per step, and were spun at 15 RPM during data collection. Variable divergence slits (VDS) were employed to ensure low background at low angle, programmed to illuminate 20mm of the sample holder. The anti-scatter slit was fixed at 1 mm above the sample surface.

GIWAXS: Grazing-Incidence Wide-Angle X-ray Scattering (GIWAXS) measurements of the Reference and Modified perovskite films on PEDOT:PSS/PET substrates were performed at the Australian Synchrotron using the SAXS/WAXS beamline with a photon energy fixed at 15 keV and an in-vacuum

(< 1 × 10-5 mbar) Pilatus 2M CCD as the detector. The incidence light angle was 0.1° and the sample to detector distance was set as 600 mm.

PL measurements: PL emission spectra and decay were recorded using a luminescence spectrometer (Edinburgh Instruments, FLSP920) with a pulsed diode laser as the excitation source: 466 nm, 200 kHz, ~100 ps pulse-width, ~0.1 nJ cm^{-2}. Sample excitation and PL emission detection was from the coated side of the samples.

PL imaging: Spatially resolved photoluminescence (PL) imaging of films of the Reference and Modified perovskite films on PEDOT:PSS/PET substrates were measured using a confocal microscope (Olympus, IX71/FV300) equipped with a fluorescence spectrometer. The 500 nm excitation beam generated by a super-continuum laser was focused on the front surface of films through a 10× objective lens. The PL emission collected by the same objective lens was filtered by a 610 nm high-pass filter to remove the scattered laser light.

PESA measurements: Performed using a Riken Kekei AC-2 spectrometer. For all samples a power intensity of 50 nW was used. The data is plotted as energy vs the cube root of the electron count, as defined by a power number of 0.33.

Contact angle measurement: Contact angle emasurment were conducted using Pheonix-Smart M instrument by Surface Electro Optics. Water cannot be used on PEDOT:PSS films. So, perovsktie precursor solution was chosen with a drop volume was 2.5 µl.

AFM imaging: A Bruker FastScan atomic force microscope with Icon scanning head and NanoScope 9.4 software was used to measure surface topography. Ultrasharp silicon nitride tips were used to image under ambient conditions. The tips have a typical force constant of 0.4 N m−1 and a resonant frequency of 70 kHz. Scan size of 1 µm were carried out at 0.7 Hz and 512 data points per scan line. All images were processed and linescans obtained using NanoScope Analysis 1.9 software.

EQE: Collected using bespoke equipment in an ambient atmosphere. The light source (Oriel 150 W Xe lamp) was chopped at 27 Hz and the electrical signal was collected under short circuit conditions using a low noise current pre-amplifier (SR570, Stanford Research Systems) and lock-in amplifier (SR830 DSP, Stanford Research Systems). A standard, filtered Si cell from Peccell Limited, which was cross-calibrated with a standard reference cell traceable to the NREL, was used as the reference.

PV properties: J-V measurements were performed at 1000 W m $^{-2}$ AM 1.5G illumination conditions using a 1 kW Oriel solar simulator as the light source in conjunction with a Keithley 2400 source measurement unit. For accurate measurement, the light intensity was calibrated using a reference silicon solar cell (PV Measurements Inc.) certified by the National Renewable Energy Laboratory. The solar simulator was in a glovebox. Devices were scanned in reverse and forward directions from 1.00 to -0.02 V, with 20 mV steps.

Supporting Information

Supporting Information is available from the Wiley Online Library or from the author.

Acknowledgements

This work was largely funded by a collaboration grant from the Australian Centre of Advanced Photovoltaics (ACAP), which is funded by the Australian Government through the Australian Renewable Energy Agency (ARENA). D.A., M.G., A.S.R.C. and A.D.S. acknowledge support from the ACAP program and the Devices and Engineered Systems Program of CSIRO Manufacturing. F.Z. and K.P.G. thank funding support from the ARC Centre of Excellence in Exciton Science (CE170100026) and ACAP. J.E. acknowledges funding from the ARC Discovery Project DP200103070.

Conflict of Interest

The authors declare no conflict of interest.

Keywords

perovskite solar cells, flexible, roll-to-roll, slot-die coating, hot-deposition, triple-cation perovskite, inverted, ambient

References

[1] A. Kojima, K. Teshima, Y. Shirai, T. Miyasaka, *J. Am. Chem. Soc.* **2009**, *131*, 6050.

[2] M. Yang, Z. Li, M. O. Reese, O. G. Reid, D. H. Kim, S. Siol, T. R. Klein, Y. Yan, J. J. Berry, M. F. A. M. van Hest, K. Zhu, *Nat. Energy* **2017**, *2*, 17038.

[3] M. Grätzel, *Nat. Mater.* **2014**, *13*, 838.

[4] M. A. Green, A. Ho-Baillie, H. J. Snaith, *Nat. Photonics* **2014**, *8*, 506.

[5] N.-G. Park, M. Grätzel, T. Miyasaka, K. Zhu, K. Emery, *Nat. Energy* **2016**, *1*, 16152.

[6] J.-P. Correa-Baena, M. Saliba, T. Buonassisi, M. Grätzel, A. Abate, W. Tress, A. Hagfeldt, *Science (80-.).* **2017**, *358*, 739 LP.

[7] S. De Wolf, J. Holovsky, S.-J. Moon, P. Löper, B. Niesen, M. Ledinsky, F.-J. Haug, J.-H. Yum, C. Ballif, *J.*

Phys. Chem. Lett. **2014**, *5*, 1035.

[8] E. M. Hutter, G. E. Eperon, S. D. Stranks, T. J. Savenije, *J. Phys. Chem. Lett.* **2015**, *6*, 3082.

[9] S. D. Stranks, G. E. Eperon, G. Grancini, C. Menelaou, M. J. P. Alcocer, T. Leijtens, L. M. Herz, A. Petrozza, H. J. Snaith, *Science (80-.).* **2013**, *342*, 341 LP.

[10] **N.d.**

[11] G. Schileo, G. Grancini, *J. Phys. Energy* **2020**, *2*, 21005.

[12] F. Bella, G. Griffini, J.-P. Correa-Baena, G. Saracco, M. Grätzel, A. Hagfeldt, S. Turri, C. Gerbaldi, *Science (80-.).* **2016**, *354*, 203 LP.

[13] A. J. Knight, A. D. Wright, J. B. Patel, D. P. McMeekin, H. J. Snaith, M. B. Johnston, L. M. Herz, *ACS Energy Lett.* **2019**, *4*, 75.

[14] N. K. Noel, S. D. Stranks, A. Abate, C. Wehrenfennig, S. Guarnera, A.-A. Haghighirad, A. Sadhanala, G. E. Eperon, S. K. Pathak, M. B. Johnston, A. Petrozza, L. M. Herz, H. J. Snaith, *Energy Environ. Sci.* **2014**, *7*, 3061.

[15] A. Abate, *Joule* **2017**, *1*, 659.

[16] Z. Li, T. R. Klein, D. H. Kim, M. Yang, J. J. Berry, M. F. A. M. van Hest, K. Zhu, *Nat. Rev. Mater.* **2018**, *3*, 18017.

[17] F. Mathies, E. J. W. List-Kratochvil, E. L. Unger, *Energy Technol.* **2020**, *8*, 1900991.

[18] H. Li, C. Zuo, A. D. Scully, D. Angmo, J. Yang, M. Gao, *Flex. Print. Electron.* **2020**, *5*, 14006.

[19] L. Han, *Nat. Energy* **2018**, *3*, 545.

[20] Y. Y. Kim, T.-Y. Yang, R. Suhonen, A. Kemppainen, K. Hwang, N. J. Jeon, J. Seo, *Nat. Commun.* **2020**, *11*, 5146.

[21] R. Patidar, D. Burkitt, K. Hooper, D. Richards, T. Watson, *Mater. today Commun.* **2020**, *22*, 100808.

[22] D. Angmo, G. DeLuca, A. D. Scully, A. S. R. Chesman, A. Seeber, C. Zuo, D. Vak, U. Bach, M. Gao, *Cell Reports Phys. Sci.* **2021**, *2*, 100293.

[23] C. Roldán-Carmona, O. Malinkiewicz, A. Soriano, G. Mínguez Espallargas, A. Garcia, P. Reinecke, T. Kroyer, M. I. Dar, M. K. Nazeeruddin, H. J. Bolink, *Energy Environ. Sci.* **2014**, *7*, 994.

[24] C. Zuo, D. Vak, D. Angmo, L. Ding, M. Gao, *Nano Energy* **2018**, *46*, 185.

[25] J.-E. Kim, S.-S. Kim, C. Zuo, M. Gao, D. Vak, D.-Y. Kim, *Adv. Funct. Mater.* **2019**, *29*, 1809194.

[26] N. Ahn, K. Kwak, M. S. Jang, H. Yoon, B. Y. Lee, J.-K. Lee, P. V Pikhitsa, J. Byun, M. Choi, *Nat. Commun.* **2016**, *7*, 13422.

[27] X. Zhao, N.-G. Park, *Photonics* **2015**, *2*, 1139.

[28] C. C. Boyd, R. Cheacharoen, T. Leijtens, M. D. McGehee, *Chem. Rev.* **2019**, *119*, 3418.

[29] D. Vak, K. Hwang, A. Faulks, Y.-S. Jung, N. Clark, D.-Y. Kim, G. J. Wilson, S. E. Watkins, *Adv. Energy Mater.* **2015**, *5*, 1401539.

[30] D. Angmo, X. Peng, J. Cheng, M. Gao, N. Rolston, K. Sears, C. Zuo, J. Subbiah, S. S. Kim, H. Weerasinghe, R. H. Dauskardt, D. Vak, *ACS Appl. Mater. Interfaces* **2018**, *10*, 22143.

[31] J. Ding, Q. Han, Q.-Q. Ge, D.-J. Xue, J.-Y. Ma, B.-Y. Zhao, Y.-X. Chen, J. Liu, D. B. Mitzi, J.-S. Hu, *Joule* **2019**, *3*, 402.

[32] M. Zhang, J. S. Yun, Q. Ma, J. Zheng, C. F. J. Lau, X. Deng, J. Kim, D. Kim, J. Seidel, M. A. Green, S. Huang,

A. W. Y. Ho-Baillie, *ACS Energy Lett.* **2017**, *2*, 438.

[33] Y. Wang, J. Wu, P. Zhang, D. Liu, T. Zhang, L. Ji, X. Gu, Z. David Chen, S. Li, *Nano Energy* **2017**, *39*, 616.

[34] H. Chen, *Adv. Funct. Mater.* **2017**, *27*, 1605654.

[35] W. Nie, H. Tsai, R. Asadpour, J.-C. Blancon, A. J. Neukirch, G. Gupta, J. J. Crochet, M. Chhowalla, S. Tretiak, M. A. Alam, H.-L. Wang, A. D. Mohite, *Science (80-.).* **2015**, *347*, 522 LP.

[36] Y.-S. Jung, K. Hwang, Y.-J. Heo, J.-E. Kim, D. Vak, D.-Y. Kim, *Adv. Opt. Mater.* **2018**, *6*, 1701182.

[37] J. F. Benitez-Rodriguez, D. Chen, M. Gao, R. A. Caruso, *Sol. RRL* **2021**, *5*, 2100341.

[38] M. Soldera, Q. Wang, F. Soldera, V. Lang, A. Abate, A. F. Lasagni, *Adv. Eng. Mater.* **2020**, *22*, 1901217.

[39] W. Nie, H. Tsai, R. Asadpour, J.-C. Blancon, A. J. Neukirch, G. Gupta, J. J. Crochet, M. Chhowalla, S. Tretiak, M. A. Alam, H.-L. Wang, A. D. Mohite, *Science* **2015**, *347*, 522.

[40] A. Al Mamun, T. T. Ava, T. M. Abdel-Fattah, H. J. Jeong, M. S. Jeong, S. Han, H. Yoon, G. Namkoong, *Sol. Energy* **2019**, *188*, 609.

[41] H.-C. Liao, P. Guo, C.-P. Hsu, M. Lin, B. Wang, L. Zeng, W. Huang, C. M. M. Soe, W.-F. Su, M. J. Bedzyk, M. R. Wasielewski, A. Facchetti, R. P. H. Chang, M. G. Kanatzidis, T. J. Marks, *Adv. Energy Mater.* **2017**, *7*, 1601660.

[42] C. Zuo, A. D. Scully, W. L. Tan, F. Zheng, K. P. Ghiggino, D. Vak, H. Weerasinghe, C. R. McNeill, D. Angmo, A. S. R. Chesman, M. Gao, *Commun. Mater.* **2020**, *1*, 33.

[43] B. Dou, J. B. Whitaker, K. Bruening, D. T. Moore, L. M. Wheeler, J. Ryter, N. J. Breslin, J. J. Berry, S. M. Garner, F. S. Barnes, S. E. Shaheen, C. J. Tassone, K. Zhu, M. F. A. M. Van Hest, *ACS Energy Lett.* **2018**, *3*, 2558.

[44] Y. Galagan, F. Di Giacomo, H. Gorter, G. Kirchner, I. de Vries, R. Andriessen, P. Groen, *Adv. Energy Mater.* **2018**, *8*, 1.

[45] M. Saliba, T. Matsui, J.-Y. Seo, K. Domanski, J.-P. Correa-Baena, M. K. Nazeeruddin, S. M. Zakeeruddin, W. Tress, A. Abate, A. Hagfeldt, M. Grätzel, *Energy Environ. Sci.* **2016**, *9*, 1989.

[46] X. Zheng, Y. Hou, C. Bao, J. Yin, F. Yuan, Z. Huang, K. Song, J. Liu, J. Troughton, N. Gasparini, C. Zhou, Y. Lin, D. J. Xue, B. Chen, A. K. Johnston, N. Wei, M. N. Hedhili, M. Wei, A. Y. Alsalloum, P. Maity, B. Turedi, C. Yang, D. Baran, T. D. Anthopoulos, Y. Han, Z. H. Lu, O. F. Mohammed, F. Gao, E. H. Sargent, O. M. Bakr, *Nat. Energy* **2020**, *5*, 131.

[47] J. Dagar, M. Fenske, A. Al-Ashouri, C. Schultz, B. Li, H. Köbler, R. Munir, G. Parmasivam, J. Li, I. Levine, A. Merdasa, L. Kegelmann, H. Näsström, J. A. Marquez, T. Unold, D. M. Többens, R. Schlatmann, B. Stegemann, A. Abate, S. Albrecht, E. Unger, *ACS Appl. Mater. Interfaces* **2021**, *13*, 13022.

[48] L. A. Castriotta, R. Fuentes Pineda, V. Babu, P. Spinelli, B. Taheri, F. Matteocci, F. Brunetti, K. Wojciechowski, A. Di Carlo, *ACS Appl. Mater. Interfaces* **2021**, *13*, 29576.

[49] X. Lin, D. Cui, X. Luo, C. Zhang, Q. Han, Y. Wang, L. Han, *Energy Environ. Sci.* **2020**, *13*, 3823.

[50] P. Caprioglio, C. M. Wolff, O. J. Sandberg, A. Armin, B. Rech, S. Albrecht, D. Neher, M. Stolterfoht, *Adv. Energy Mater.* **2020**, *10*, 2000502.

[51] P. Caprioglio, M. Stolterfoht, C. M. Wolff, T. Unold, B. Rech, S. Albrecht, D. Neher, *Adv. Energy Mater.* **2019**, *9*, 1901631.

[52] C. M. Wolff, P. Caprioglio, M. Stolterfoht, D. Neher, *Adv. Mater.* **2019**, *31*, 1902762.

[53] F. C. Krebs, *Sol. Energy Mater. Sol. Cells* **2009**, *93*, 394.

[54] T. Liu, K. Chen, Q. Hu, R. Zhu, Q. Gong, *Adv. Energy Mater.* **2016**, *6*, 1600457.

[55] A. Al-Ashouri, A. Magomedov, M. Roß, M. Jošt, M. Talaikis, G. Chistiakova, T. Bertram, J. A. Márquez, E. Köhnen, E. Kasparavičius, S. Levcenco, L. Gil-Escrig, C. J. Hages, R. Schlatmann, B. Rech, T. Malinauskas, T. Unold, C. A. Kaufmann, L. Korte, G. Niaura, V. Getautis, S. Albrecht, *Energy Environ. Sci.* **2019**, *12*, 3356.

[56] E. A. Alharbi, M. I. Dar, N. Arora, M. H. Alotaibi, Y. A. Alzhrani, P. Yadav, W. Tress, A. Alyamani, A. Albadri, S. M. Zakeeruddin, M. Grätzel, *Res. (Washington, D.C.)* **2019**, *2019*, 8474698.

[57] D. Qian, Z. Zheng, H. Yao, W. Tress, T. R. Hopper, S. Chen, S. Li, J. Liu, S. Chen, J. Zhang, X.-K. Liu, B. Gao, L. Ouyang, Y. Jin, G. Pozina, I. A. Buyanova, W. M. Chen, O. Inganäs, V. Coropceanu, J.-L. Bredas, H. Yan, J. Hou, F. Zhang, A. A. Bakulin, F. Gao, *Nat. Mater.* **2018**, *17*, 703.

[58] W. Tress, *Adv. Energy Mater.* **2017**, *7*, 1602358.

[59] J.-P. Correa-Baena, W. Tress, K. Domanski, E. H. Anaraki, S.-H. Turren-Cruz, B. Roose, P. P. Boix, M. Grätzel, M. Saliba, A. Abate, A. Hagfeldt, *Energy Environ. Sci.* **2017**, *10*, 1207.

[60] J. Siekmann, S. Ravishankar, T. Kirchartz, *ACS Energy Lett.* **2021**, 3244.

[61] O. Graydon, *Nat. Photonics* **2016**, *10*, 145.

[62] N. De Marco, H. Zhou, Q. Chen, P. Sun, Z. Liu, L. Meng, E.-P. Yao, Y. Liu, A. Schiffer, Y. Yang, *Nano Lett.* **2016**, *16*, 1009.

[63] R. J. Stoddard, A. Rajagopal, R. L. Palmer, I. L. Braly, A. K.-Y. Jen, H. W. Hillhouse, *ACS Energy Lett.* **2018**, *3*, 1261.

[64] A. D. Jodlowski, C. Roldán-Carmona, G. Grancini, M. Salado, M. Ralaiarisoa, S. Ahmad, N. Koch, L. Camacho, G. de Miguel, M. K. Nazeeruddin, *Nat. Energy* **2017**, *2*, 972.

[65] S. Wu, Z. Li, J. Zhang, T. Liu, Z. Zhu, A. K.-Y. Jen, *Chem. Commun.* **2019**, *55*, 4315.

[66] M. V Khenkin, E. A. Katz, A. Abate, G. Bardizza, J. J. Berry, C. Brabec, F. Brunetti, V. Bulović, Q. Burlingame, A. Di Carlo, R. Cheacharoen, Y.-B. Cheng, A. Colsmann, S. Cros, K. Domanski, M. Dusza, C. J. Fell, S. R. Forrest, Y. Galagan, D. Di Girolamo, M. Grätzel, A. Hagfeldt, E. von Hauff, H. Hoppe, J. Kettle, H. Köbler, M. S. Leite, S. (Frank) Liu, Y.-L. Loo, J. M. Luther, C.-Q. Ma, M. Madsen, M. Manceau, M. Matheron, M. McGehee, R. Meitzner, M. K. Nazeeruddin, A. F. Nogueira, Ç. Odabaşı, A. Osherov, N.-G. Park, M. O. Reese, F. De Rossi, M. Saliba, U. S. Schubert, H. J. Snaith, S. D. Stranks, W. Tress, P. A. Troshin, V. Turkovic, S. Veenstra, I. Visoly-Fisher, A. Walsh, T. Watson, H. Xie, R. Yıldırım, S. M. Zakeeruddin, K. Zhu, M. Lira-Cantu, *Nat. Energy* **2020**, *5*, 35.

[67] W. Tress, K. Domanski, B. Carlsen, A. Agarwalla, E. A. Alharbi, M. Graetzel, A. Hagfeldt, *Nat. Energy* **2019**, *4*, 568.

[68] K. Domanski, E. A. Alharbi, A. Hagfeldt, M. Grätzel, W. Tress, *Nat. Energy* **2018**, *3*, 61.

[69] N. Arora, M. I. Dar, A. Hinderhofer, N. Pellet, F. Schreiber, S. M. Zakeeruddin, M. Grätzel, *Science (80-.).* **2017**, *358*, 768.

[70] Z. Liang, S. Zhang, X. Xu, N. Wang, J. Wang, X. Wang, Z. Bi, G. Xu, N. Yuan, J. Ding, *RSC Adv.* **2015**, *5*, 60562.

[71] T. A. S. Doherty, A. J. Winchester, S. Macpherson, D. N. Johnstone, V. Pareek, E. M. Tennyson, S. Kosar, F. U. Kosasih, M. Anaya, M. Abdi-jalebi, Z. Andaji-garmaroudi, E. L. Wong, J. Madéo, Y. Chiang, J. Park, Y. Jung, C. E. Petoukhoff, G. Divitini, M. K. L. Man, C. Ducati, A. Walsh, P. A. Midgley, K. Dani, S. D. Stranks, **2020**, *580*, DOI 10.1038/s41586-020-2184-1.

[72] Y. Sun, J. Peng, Y. Chen, Y. Yao, Z. Liang, *Sci. Rep.* **2017**, *7*, 46193.

[73] X. Wang, Y. Fan, L. Wang, C. Chen, Z. Li, R. Liu, H. Meng, Z. Shao, X. Du, H. Zhang, G. Cui, S. Pang, *Chem* **2020**, *6*, 1369.

[74] L. H. Rossander, T. T. Larsen-Olsen, H. F. Dam, T. M. Schmidt, M. Corazza, K. Norrman, I. Rajkovic, J. W. Andreasen, F. C. Krebs, *CrystEngComm* **2016**, *18*, 5083.

[75] M. Qin, K. Tse, T.-K. Lau, Y. Li, C.-J. Su, G. Yang, J. Chen, J. Zhu, U.-S. Jeng, G. Li, H. Chen, X. Lu, *Adv. Mater.* **2019**, *31*, 1901284.

[76] L.-Q. Xie, L. Chen, Z.-A. Nan, H.-X. Lin, T. Wang, D.-P. Zhan, J.-W. Yan, B.-W. Mao, Z.-Q. Tian, *J. Am. Chem. Soc.* **2017**, *139*, 3320.

[77] S. Kavadiya, J. Strzalka, D. M. Niedzwiedzki, P. Biswas, *J. Mater. Chem. A* **2019**, *7*, 12790.

[78] N. J. Jeon, J. H. Noh, Y. C. Kim, W. S. Yang, S. Ryu, S. Il Seok, *Nat. Mater.* **2014**, *13*, 897.

[79] M. Abdelsamie, T. Li, F. Babbe, J. Xu, Q. Han, V. Blum, C. M. Sutter-Fella, D. B. Mitzi, M. F. Toney, *ACS Appl. Mater. Interfaces* **2021**, *13*, 13212.

[80] J. C. Hamill, J. Schwartz, Y.-L. Loo, *ACS Energy Lett.* **2018**, *3*, 92.

[81] S. A. Kulkarni, T. Baikie, P. P. Boix, N. Yantara, N. Mathews, S. Mhaisalkar, *J. Mater. Chem. A* **2014**, *2*, 9221.

[82] M. Jaysankar, W. Qiu, J. Bastos, J. G. Tait, M. Debucquoy, U. W. Paetzold, D. Cheyns, J. Poortmans, *J. Mater. Chem. A* **2016**, *4*, 10524.

[83] R. Prasanna, A. Gold-Parker, T. Leijtens, B. Conings, A. Babayigit, H.-G. Boyen, M. F. Toney, M. D. McGehee, *J. Am. Chem. Soc.* **2017**, *139*, 11117.

[84] E. V. Peán, S. Dimitrov, C. S. De Castro, M. L. Davies, *Phys. Chem. Chem. Phys.* **2020**, *22*, 28345.

[85] F. Zheng, X. Wen, T. Bu, S. Chen, J. Yang, W. Chen, F. Huang, Y. Cheng, B. Jia, *ACS Appl. Mater. Interfaces* **2018**, *10*, 31452.

[86] J. Haddad, B. Krogmeier, B. Klingebiel, L. Krückemeier, S. Melhem, Z. Liu, J. Hüpkes, S. Mathur, T. Kirchartz, *Adv. Mater. Interfaces* **2020**, *7*, 2000366.

[87] M. Abdi-Jalebi, M. Ibrahim Dar, S. P. Senanayak, A. Sadhanala, Z. Andaji-Garmaroudi, L. M. Pazos-Outón, J. M. Richter, A. J. Pearson, H. Sirringhaus, M. Grätzel, R. H. Friend, *Sci. Adv.* **2019**, *5*, DOI 10.1126/sciadv.aav2012.

[88] M. Stolterfoht, C. M. Wolff, J. A. Márquez, S. Zhang, C. J. Hages, D. Rothhardt, S. Albrecht, P. L. Burn, P. Meredith, T. Unold, D. Neher, *Nat. Energy* **2018**, *3*, 847.

[89] S. Akin, N. Arora, S. M. Zakeeruddin, M. Grätzel, R. H. Friend, M. I. Dar, *Adv. Energy Mater.* **2020**, *10*, 1903090.

[90] P. Schulz, *ACS Energy Lett.* **2018**, *3*, 1287.

[91] V. Sarritzu, N. Sestu, D. Marongiu, X. Chang, S. Masi, A. Rizzo, S. Colella, F. Quochi, M. Saba, A. Mura, G. Bongiovanni, *Sci. Rep.* **2017**, *7*, 44629.

TOC

Roll-to-roll fabrication of perovskite solar cells (PSCs) on flexible substrates represents a promising approach for commercialization. By using a triple cation perovskite and a novel passivation strategy by doping guanidinium iodide into PEDOT:PSS, we demonstrate slot-die coated PSCs under ambient environment enables millimeter-sized perovskite clusters, leading to a record PCE of 12%.

M. Othman, F. Zheng, A. Seeber, A. S. R. Chesman, A. D. Scully, K. P. Ghiggino, M. Gao, J. Etheridge,* D. Angmo*

Millimeter-sized Clusters of Triple Cation Perovskite Enables Highly Efficient and Reproducible Roll-to-Roll Fabricated Inverted Perovskite Solar Cells